ELSEVIER

J. Non-Newtonian Fluid Mech. 86 (1999) 61–88

Journal of Non-Newtonian Fluid Mechanics

Extensional flow of a polystyrene Boger fluid through a 4 : 1 : 4 axisymmetric contraction/expansion

Jonathan P. Rothstein, Gareth H. McKinley*

Department of Mechanical Engineering, Massachusetts Institute of Technology, Cambridge, MA 02139, USA

Received 6 June 1998; received in revised form 15 September 1998

Abstract

The creeping flow of a dilute (0.025 wt%) monodisperse polystyrene/polystyrene Boger fluid through a 4 : 1 : 4 axisymmetric contraction/expansion is experimentally observed for a wide range of Deborah numbers. Pressure drop measurements across the orifice plate show a large extra pressure drop that increases monotonically with Deborah number above the value observed for a similar Newtonian fluid at the same flow rate. This enhancement in the dimensionless pressure drop is not associated with the onset of a flow instability, yet it is not predicted by existing steady-state or transient numerical computations with simple dumbbell models. It is conjectured that this extra pressure drop is the result of an additional dissipative contribution to the polymeric stress arising from a *stress-conformation hysteresis* in the strong non-homogeneous extensional flow near the contraction plane. Such a hysteresis has been independently measured and computed in recent studies of homogeneous transient uniaxial stretching of PS/PS Boger fluids [Doyle et al., J. Non-Newtonian Fluid Mech. 76 (1998)]. Flow visualization and velocity field measurements using digital particle image velocimetry (DPIV) show large upstream growth of the corner vortex with increasing Deborah number. At large Deborah numbers, the onset of an elastic instability is observed, first locally as small amplitude fluctuations in the pressure measurements, and then globally as an azimuthal precessing of the upstream corner vortex accompanied by periodic oscillations in the pressure drop across the orifice.

Keywords: Axisymmetric contraction; Couette correction; Entrance pressure drop; Dissipative stress; Polystyrene Boger fluid

1. Introduction

Recent experimental and numerical investigations have shown that the dynamical evolution of the microstructure in dilute polymer solutions undergoing a strong extensional flow is far more complex than the qualitative picture of a single dumbbell undergoing uniaxial stretching. Fluorescence imaging of individual DNA molecules by Chu and coworkers has shown that a number of distinct conformational trajectories are possible in an extensional flow. Some molecules do indeed resemble

* Corresponding author.

0377-0257/99/$ – see front matter
PII: S0377-0257(98)00202-X

dumbbells undergoing elongation, however, many other conformations such as 'half-dumbbells', 'kinked chains' and 'folded' molecules are also observed [1]. Macroscopic quantities such as polymeric stress and birefringence depend on differently-weighted ensemble averages of these possible microscopic configurations. One may therefore expect the stress-strain characteristics of a dilute polymer solution undergoing transient uniaxial elongation to be more complex than that predicted by a simple dumbbell model which only captures a single measure of the end-to-end chain length.

Doyle et al. have recently shown through combined birefringence, tensile stress measurements and Brownian dynamics calculations that a dilute monodisperse PS solution undergoing uniaxial extension in a filament stretching device exhibits a pronounced *stress-conformation hysteresis* [2]. That is, the stress and the end-to-end conformation (as measured by phase-modulated birefringence) evolve along one path during the transient unraveling process and a distinct second path during the relaxation back to equilibrium. The difference in these curves represents an additional energy loss associated with a hydrodynamic coupling between the externally imposed flow and the internal conformational chain dynamics which appears to only be significant when the fluid is subjected to a strong flow and large Hencky strains. Similar hysteretic effects have been observed in Brownian dynamics calculations of ensembles of bead-rod chains [2,3] and FENE dumbbells [4] and can be captured, at least qualitatively, in simple closed-form constitutive models such as the ones recently proposed by Hinch [5] and Rallison [3]. The first qualitative discussion of such ideas together with scaling estimates of the magnitudes of the resulting stress was given by Ryskin [6] in his analysis of the pressure drop measurements of King and James for sink flows of dilute polymer solutions at high Reynolds numbers. This hysteresis gives rise to an additional contribution to the polymer stress which may be modeled as purely viscous (i.e. it disappears instantaneously upon the cessation of stretching) [7] or as viscoelastic in origin with a very short characteristic relaxation time [2]. Regardless of these distinctions we refer to this phenomenon as arising from an additional polymeric *dissipative stress* which removes energy from the flow. In a complex flow containing regions of extension and shear, the effects of this dissipative stress will be reflected in macroscopic observations of dynamic quantities such as pressure drops or drag coefficients.

In the present work we investigate the enhancement in the pressure drop arising from the strong converging–diverging flow of a dilute polymer solution at low Reynolds number through a 4 : 1 : 4 axisymmetric contraction/expansion. The basic orifice plate geometry for flow through an axisymmetric contraction/expansion can be seen in Fig. 1. A fully-developed flow through a tube of radius R_1 is accelerated through an abrupt contraction of radius R_2 and is then rapidly re-expanded into a second tube of the upstream radius R_1. In the process, a secondary recirculating flow may develop in the corners directly upstream and/or downstream of contraction. The elasticity of the fluid plays an important role in the flow structure and in the vortex formation and growth. The relative importance of the fluid elasticity is characterized by the Deborah number, $\mathrm{De} \equiv \lambda/\mathscr{T}$, where λ is a characteristic relaxation time of the fluid and $\mathscr{T}$ is the characteristic timescale of the flow (eg. residence time in the contraction region). The flow through a contraction is a complex flow with shearing deformation near the walls and a strong nonhomogeneous extensional flow along the centerline and within close proximity of the contraction plane. For highly viscoelastic fluids, the recirculation region in the corners upstream of the contraction can be very strong and readily observable [8]. For this reason and because of the geometric simplicity of the problem, viscoelastic flow through a contraction has become a standard numerical benchmark for non-Newtonian fluid dynamics calculations [9].

There is a great deal of literature, both experimental and numerical, dealing with flow through a contraction over a wide range of Deborah numbers and contraction ratios using a large variety of fluids

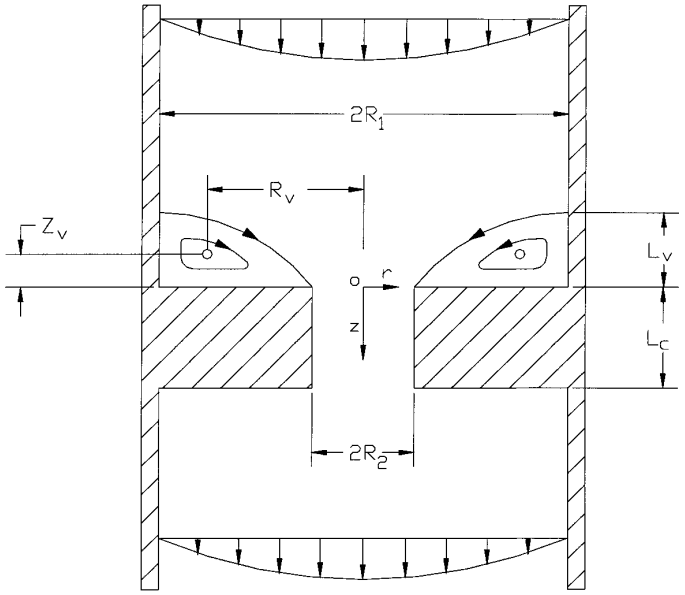

Fig. 1. Schematic diagram of contraction geometry and definitions of important length scales.

and constitutive models. The experimental work has been reviewed in detail by both Boger [10] and White et al. [11] and hence we will only briefly describe some of the global characteristics observed in highly elastic polymer solutions. At low Deborah numbers, the streamlines near the contraction plane are identical to those observed in creeping flow of a Newtonian fluid with a weak 'Moffatt eddy' present in the outer stagnant corner of the upstream and downstream tube. As the Deborah number is increased, two distinctly different sequences of flow patterns can be observed for a particular contraction ratio. For some elastic fluids (eg. PAA/CS Boger fluids in a 4 : 1 contraction [10,12]) the upstream corner vortex increases in strength and grows radially inward toward the re-entrant corner while the reattachment point grows steadily upstream. This flow regime is steady in time and substantial upstream vortex growth is observed as the Deborah number is further increased. In this case, numerical computations are able to quantitatively capture the kinematic characteristics of the flow [13,14]. However, for other fluids (e.g. PIP/PB Boger fluids in a 4 : 1 contraction) the corner vortex decreases in size as the Deborah number is increased and a separate, distinct 'lip' vortex [10] forms near the re-entrant corner. The subsequent upstream vortex growth observed at higher Deborah numbers originates from outward radial growth of the lip vortex. Experimental measurements [15,16] show that these flows are unsteady in time and three dimensional in nature. Successful simulations of a time-dependent lip vortex in an axisymmetric contraction have yet to be performed, although similar transient phenomena have been recently computed in three dimensional planar contraction geometries [17].

At very high Deborah numbers, the large upstream vortex observed for either of the fluid formulations described above becomes unstable to a global dynamical mode that is a sensitive function of the contraction ratio [15,16] and is reminiscent of the melt flow instabilities observed in polymer melts [11]. These global flow instabilities have serious repercussions for industrial applications such as extrusion and injection molding where the quality of the extrudate and the flow rate are important

design criteria. One of the goals of the present study is to investigate which vortex evolution pathway is followed by a dilute and monodisperse polystyrene Boger fluid which has been well characterized in both shear and extension. Polystyrene Boger fluids are purely organic in formulation like PIB/PB fluids with none of the hydrogen-bonding and polyelectrolyte issues that affect aqueous PAA solutions, but the local chain architecture is more rigid than PIB as a result of the styrene side groups. This leads to longer Kuhn statistical segment lengths in dilute solution and higher values of molecular weight between entanglements in concentrated solutions and melts of polystyrene [18]. It is, therefore, not clear a priori which vortex evolution pathway to expect for a PS/PS Boger fluid.

The difference in the sequence of flow transitions for two different fluids that are ostensibly identical in shear must arise from differences in the extensional rheology. It is conjectured that these differences arise from the molecular characteristics of the *equilibrium* conformations of the PAA and PIB chains [12]. Such conformational differences will also have a large effect on the evolution of *non-equilibrium properties* such as the transient extensional stress growth in the fluid as a function of both *strain* and *strain-rate*. In particular, the interplay between (entropic) elastic energy storage and energy dissipation during chain unraveling and the associated stress-orientation hysteresis will impact the macroscopic entrance pressure drop and the stability of the global motion as the Deborah number is increased.

Of course, observation of the fluid kinematics through flow visualization is insufficient for deducing the dynamical response of the polymeric stresses. In planar contraction flows, additional information can be obtained using pointwise birefringence and Laser Doppler Velocimetry (LDV), and these measurements can be combined to rigorously test the performance of various constitutive models [19]. The much lower Hencky strain attained in the planar geometry typically results in much less pronounced viscoelastic effects than observed in axisymmetric contractions [6]; however, application of line-of-sight techniques such as birefringence in axisymmetric geometeries is not straightforward. Recently Byars et al. [20] have combined experimental measurements of the centerline velocity gradient of a PIB/PB fluid flowing through a axisymmetric 4 : 1 contraction with independent measurements of the extensional rheology performed using a filament stretching device [21] to show that even with a multimode nonlinear model it is not possible to fit both the shear rheology and the extensional rheology of a fluid with a single set of constitutive parameters. One possible cause for this discrepancy is the existence of an additional contribution to the stress in strong extensional flows which is not captured by existing dumbbell-like constitutive models.

An alternate experimental technique which can provide some limited insight into the polymeric stresses that develop during flow through a contraction is measurement of the additional or extra pressure drop resulting from the converging/diverging flow. Pressure drop measurements for axisymmetric contraction flow of polymer solutions are not as common in the literature as visualization of flow patterns and yet they can be an effective tool for comparison of constitutive rheological predictions and for quantifying the accuracy of a numerical simulation. The majority of entrance pressure drop data have been taken as a means of estimating the extensional viscosity of a fluid [16,22–24] or to augment the information available from streak images and reattachment length measurements [25,26], while other measurements have been taken at Reynolds numbers well beyond the creeping flow limit studied here [27]. A common observation amongst these studies is that there exists an extra pressure drop associated with the flow of a viscoelastic non-Newtonian fluid across an abrupt contraction that does not exist for a Newtonian fluid; i.e. the dimensionless pressure drop across an abrupt contraction, defined as $\mathscr{P}(\mathrm{De}) = \Delta P_{\text{non-Newtonian}}(\mathrm{De},\ Q)/\Delta P_{\text{Newtonian}}(\mathrm{De} = 0,\ Q)$, increases monotonically with Deborah number.

In general, the total pressure drop across the contraction arises from the fully-developed viscous flow through the pipe plus entrance and exit effects due to the contraction. In the present experiments, an orifice plate geometry has been chosen over other types of abrupt contractions because the extended polymer chains are allowed to relax quite quickly after exiting the contraction. The measured pressure drop is then primarily a function of the dissipative stresses that remove energy from the flow across the contraction and not due to stored elastic energy in the entropic springs that gradually relaxes in the narrow downstream tube. Such a contraction/expansion geometry may be useful in probing the dissipative contributions to the polymeric stress in a prototypical complex flow where significant differences in the extra pressure drop may be observed at the same Deborah number in PAA/CS, PIB/PB and PS/PS Boger fluids with identical shear rheology. We begin with a PS/PS fluid in the present work because the existence of a stress-conformation hysteresis has already been demonstrated experimentally and numerically [2]. Furthermore, the fluid is a dilute solution of a monodisperse polymer and the results of these experiments may provide a better benchmark for theoretical comparisons than results using a similar polydisperse polymeric component.

Cartalos and Piau investigated the flow of a partially hydrolyzed polyacrylamide (HPAM) in glycerin solution through a similar orifice plate contraction/expansion [25]. In these experiments, the authors found that the dimensionless pressure drop increased monotonically with deformation rate and then began to plateau at large values between $\mathscr{P} = 8$ and $\mathscr{P} = 18$ depending on the concentration of HPAM and the presence or absence of salt.

In the numerical literature, good agreement with experiment has been obtained for both the evolution of vortex structure [14] and the upstream birefringence patterns [28]. For some fluids (eg. a molten polybutadiene rubber), the enhancement in the dimensionless pressure drop $\mathscr{P}$(De) across a contraction is well described by the computations; however, for other materials (e.g. polystyrene), the measured pressure drop is severely under predicted even though the shear rheology is well described by a multimode Leonov model [29]. In fact, for dumbbell-like models (e.g. the FENE-P and Oldroyd-B models) which describe the flow of dilute polymer solutions, a *decrease* in the dimensionless pressure drop $\mathscr{P}$(De) is predicted in most cases as the Deborah number is increased [13]. Only in the limit of high Deborah numbers and fully extended polymer molecules is a small extra pressure drop predicted numerically [30,31]. This enhancement in the dimensionless pressure drop when the molecules approach full extension is consistent with observation of entrance pressure drops for rigid rod systems [32] in which the additional non-Newtonian contribution to the extensional viscosity is explicitly dissipative because the rods cannot elongate and store energy entropically.

The systematic discrepancies between experimentally-observed entrance pressure drops and numerically-computed values arising from dissipative contributions to the total stress may play a role in other complex flows. For example, similar deviations in other integrated quantities such as the drag coefficient on spheres [33] and cylinders [34,35] have been observed for a variety of polymeric solutions. The work of Solomon and Muller showed that the enhancement in the viscoelastic drag coefficient C_D(De) for the flow of a polystyrene Boger fluid past a sphere was larger (by up to an order of magnitude) than the results of similar experiments using different polymer solutions such as PIB Boger fluids [33]. Since we use a very similar PS/PS fluid in the present work, we may expect to observe dramatic increases in pressure drop similar to those observed in the drag measurements past spheres and cylinders.

We describe our experimental apparatus and techniques in Section 2 and show that the shear rheology of the fluid is well described by the classical bead-spring model of Rouse and Zimm. In

Section 3, we first present observations of the pressure drop through a 4 : 1 : 4 orifice for a Newtonian solvent and then document the enhancement arising from the addition of the polymer. Flow visualization and DPIV are then combined with measurements of fluctuations in the pressure drop to document the onset of an elastic instability that leads to global oscillations in the flow as the Deborah number is increased.

2. Experimental

2.1. Flow geometry and experimental setup

Fig. 1 shows a schematic diagram of the contraction geometry and defines several useful length scales which we refer to extensively below. The upstream and downstream radii are denoted by the subscript 1 and 2 respectively. The length scales indicative of the vortex size and growth are described by the distance to the separation point upstream (L_v) and by the coordinates of the center of the recirculation denoted by the distance upstream of the contraction plane (Z_v) and the distance from the centerline (R_v). These distances are nondimensionalized with the diameter of the upstream tube to determine the dimensionless reattachment length $\chi \equiv L_v/2R_1$ and the dimensionless coordinates of the vortex center $\zeta \equiv Z_v/2R_1$ and $\xi \equiv R_v/2R_1$. The contraction ratio is defined as $\beta \equiv R_1/R_2$.

The experimental setup has been designed to provide a versatile mechanism for systematically studying steady and time-dependent flows of elastic liquids through abrupt contractions. A schematic diagram of the apparatus is shown in Fig. 2. A linear stepper motor (Servo Systems, Model 1000S) and microstepper controller (Intelligent Motion Systems, Model Panther LI) are utilized to drive fluid

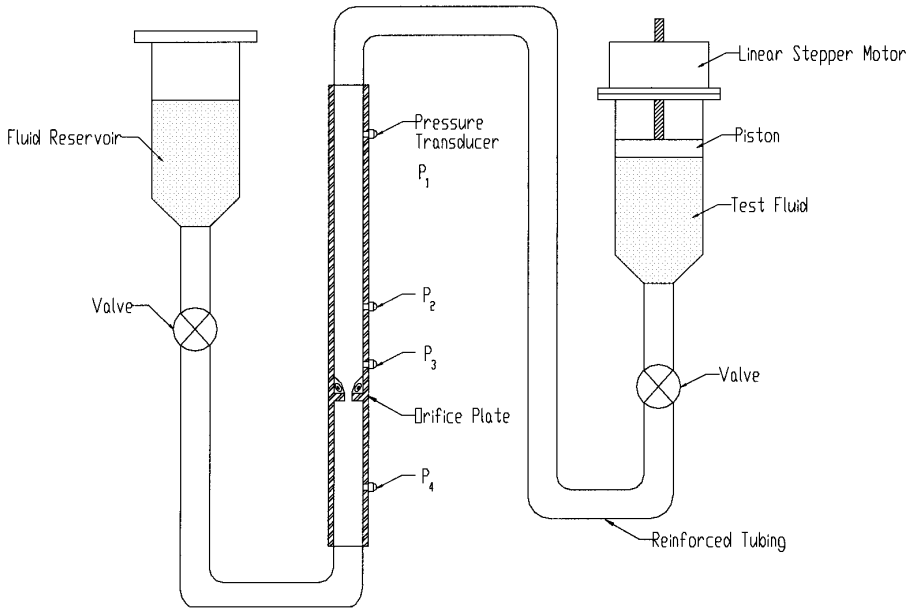

Fig. 2. Schematic diagram of the experimental apparatus.

through the system at a constant displacement rate and hence a constant volumetric flow rate Q. The fluid flows through a plexiglass tube of radius $R_1 = 1.4$ cm, past three possible pressure transducer locations and through an interchangeable orifice plate. After passing beyond the contraction plane, the fluid again passes through a short section of 1.4 cm radius tubing, past the last pressure transducer location and into a collection reservoir. When the experiment is completed the piston is retracted and the fluid is drawn in reverse back through the contraction to its original location.

The orifice plates were designed so that they could easily be replaced with a variety of different inserts containing sharp or smooth corners of various contraction ratios. In future work, this functionality will be utilized. All experiments presented in this paper are for an orifice plate with sharp corners and a contraction ratio of $\beta = 4$ because this configuration has been established as a benchmark for numerical simulations.

During each experiment, a single high-resolution pressure transducer (Endevco, Model 8510B-5) was flush mounted in one of the three upstream pressure locations and another was placed in the downstream location to measure the total pressure drop associated with flow through the contraction. The remaining upstream pressure transducer locations were sealed with screws. Table 1 shows the axial distance of each pressure transducer from the contraction plane. For clarity, it is useful to define several differential pressures by the location of the pressure transducers used. For instance, the pressure drop across the contraction between pressure transducers 2 and 4 is denoted as $\Delta P_{24} = (P_2 - P_4)$. Several different pressure transducers locations were created sufficiently far upstream of contraction plane to ensure that the pressure transducers were not affected by the presence of the elastically-driven growth of the upstream and downstream vortices.

As the flow rate is increased, the pressure transducers measure a combination of the pressure drop arising from fully-developed rectilinear flow in the straight pipe and the extra pressure drop caused by the presence of the orifice plate $\Delta P(Q) = \Delta P_{\text{straight pipe}} + \Delta P_{\text{ext}}$. We are only interested, however, in the extra pressure drop which we denote as $\Delta P'_{24}$ where the prime indicates that the contribution to the total pressure drop resulting from the Poiseuille flow in the pipe connecting the pressure transducers has been removed in order to isolate the extra pressure drop across the contraction/expansion. In other words, $\Delta P'_{24} = \Delta P_{24} - 8QL\eta/\pi R_2^4$ where $L \equiv z_4 - (z_2 + L_c)$ is the length of straight tubing between the pressure transducers and the contraction, Q is the volume flow rate of the fluid and η is the fluid viscosity. Lastly, we define a dimensionless pressure drop $\mathscr{P}(\text{De}) \equiv \Delta P'_{24}(Q, \text{De})/\Delta P'_{24}(Q, \text{De} = 0)$ where $\Delta P'_{24}(Q, \text{De} = 0)$ is the pressure drop across the orifice of the Newtonian oligomeric polystyrene oil at a given flow rate and $\Delta P'_{24}(Q, \text{De})$ is the pressure drop across the contraction/expansion of the viscoelastic 0.025% PS/PS polymer solution at the same flow rate. This dimensionless pressure drop differs from the Couette correction often used to present contraction flow pressure drop data by a constant factor and is discussed further in Section 3.1.

Table 1
Location of the flush mounted pressure transducers with respect to the contraction plane located at $z = 0$

Vortice	Pressure transducer, P_i	Distance from contraction plane, z_i (cm)
Upstream	P_1	−22.86
	P_2	−7.62
	P_3	−2.54
Downstream	P_4	+8.26

2.2. Digital particle image velocimetry

Digital particle image velocimetry (DPIV) is a non-invasive technique for acquiring measurements of velocity vector fields over an entire flow domain. DPIV measures local velocities by determining the average displacements of particles ($\overline{\Delta x}$, $\overline{\Delta y}$) in a small correlation region over a known time Δt. Two images of laser illuminated particles in a flow field are taken and broken down into correlation windows. Within each correlation window, the two frames are compared and an average displacement is calculated. This displacement is then converted into a velocity through the known time difference between images.

In these experiments, a DPIV algorithm is used to measure the axial and radial velocity components of the flow upstream of the axisymmetric contraction/expansion. A single beam from a 300 mW Ar-ion laser (Ion Laser Technologies, Model 5500A-00) is passed through a non-Gaussian optical element to obtain a 1 mm thick laser light sheet of uniform intensity. The use of a single-mode optical fiber (Oz Optics) allows the light sheet to be easily directed normal to the surface of the tube to illuminate the fluid which is seeded with 50 μm diameter silvered hollow glass spheres (Potters Industries) at a volume fraction of 2.1×10^{-3}. This concentration of particles corresponds to the number of particles required to achieve a minimum of 20–25 particles per 16×16 pixel correlation window [36]. Using Einstein's correction to the viscosity of a suspension [37] we may estimate the increase in the zero-shear-rate viscosity of the fluid as

$$\frac{\eta_{\text{suspension}}}{\eta_{\text{solvent}}} = 1 + 2.5\varphi \tag{1}$$

where η is the shear viscosity and φ is the volume fraction of particles. From Eq. (1) we can estimate that the shear viscosity of the suspension will be approximately 0.53% greater than the shear viscosity of the solvent. Subsequent measurements of the viscometric properties of the suspension showed no discernable effect of the particle addition within the accuracy of the rheological measurements.

The illuminated fluid motion is videotaped using a digital video camera (Sony DCR-VX1000) aligned orthogonal to the laser light sheet. The video recorder contains 3 CCD chips and digitally records 480×640 pixel images to tape every 0.033 s using a lossless compression algorithm. Images are then captured digitally onto the hard drive of a PC where the DPIV analysis is performed. A more detailed discussion of the utility of the DPIV technique for velocity and other kinematic measurements in non-Necwtonian fluids is given by Pakdel and McKinley [36].

2.3. Flow visualization

The same optical configuration used for the DPIV analysis was also utilized for direct flow visualization. Digital video of the laser illuminated flow field was recorded and used to artificially generate long time exposures or 'streak' images from multiple single frames. These 'streak' images were used to record the streamlines in the flow field and were created by first thresholding many frames to remove all background light and then averaging all the images together. The resulting image is similar to the classic streak images created by exposing photographic film over a long period of time. This flow visualization technique has been used extensively for contraction flows and other complex flows throughout the field of non-Newtonian fluid dynamics [8].

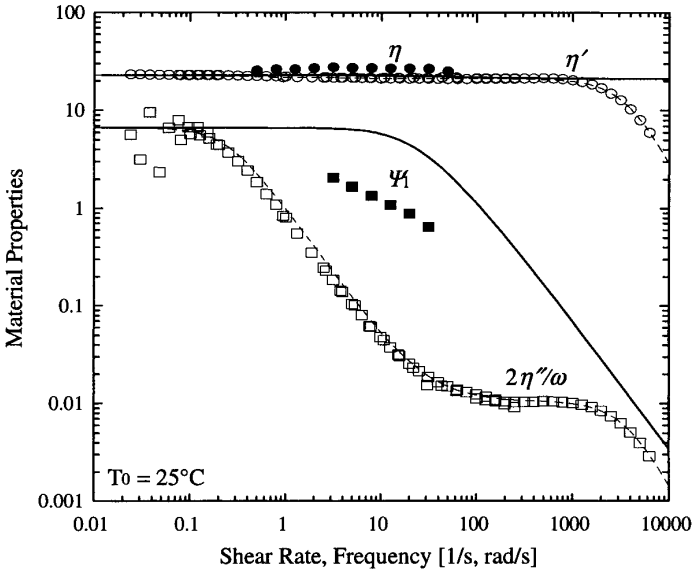

Fig. 3. Rheological material functions of the 0.025 wt.% monodisperse polystyrene in oligomeric polystyrene solution. The data includes: ●, steady shear viscosity $\eta(\dot{\gamma})$ (Pa s); ○, dynamic viscosity $\eta'(\omega)$ (Pa s); □ dynamic rigidity $2\eta''(\omega)/\omega$ (Pa s^2); ■, first normal stress coefficient $\Psi_1(\dot{\gamma})$ (Pa s^2); and the corresponding FENE-P and Zimm model fits plotted as solid lines '———' and dashed lines '- -' respectively.

2.4. Fluid rheology

The viscoelastic fluid consists of an 0.025 wt.% solution of monodisperse polystyrene (PS) (Scientific Polymer Products) with a molecular weight of 2.25×10^6 g/mol and polydispersity of 1.03. The polystyrene is dissolved in oligomeric styrene (Hercules) to yield a dilute solution with $c/c^* = 0.24$. The resulting solution falls into a class of fluids first described in detail by Boger [38] which are highly elastic with an almost constant viscosity. The absence of shear thinning in the viscosity allows one to investigate elastic effects of the fluid alone, while the large viscosities and long relaxation times eliminate inertial effects while permitting flows to be studied at high Deborah numbers. The use of a monodisperse polymeric constituent in the PS/PS fluid permits the rheology to be more easily compared with molecular theories for dilute solutions.

Fig. 3 shows a master curve of the rheological properties for the 0.025% PS/PS solution at $T_0 = 25^\circ$C, measured with a controlled stress device (TA Instruments, Model AR1000N). The viscoelastic properties of the fluid are characterized in small amplitude oscillatory shear flow by the dynamic viscosity $\eta'(\omega)$ and the dynamic rigidity $2\eta''(\omega)/\omega$ which are both functions of the frequency of oscillation. In steady shear flow the fluid is characterized by the first normal stress coefficient $\Psi_1(\dot{\gamma}) = (\tau_{11} - \tau_{22})/\dot{\gamma}^2$ and viscosity $\eta(\dot{\gamma})$, each of which are functions of the shear rate. Fig. 3 shows that the viscosity of the solution is approximately constant over several decades of shear rate. The fluid is strongly elastic and its first normal stress coefficient shear thins monotonically throughout the entire range over which data can be obtained.

The linear viscoelastic properties are well described by the Rouse–Zimm bead-spring model [39] with a longest relaxation time of $\lambda_z = 3.24$ s. The Rouse–Zimm model also predicts a zero-shear-rate

viscosity of $\eta_0 = 22.8$ Pa s, nearly all of which is contributed by the oligomeric PS solvent ($\eta_s = 21.0$ Pa s), and a first normal stress coefficient of $\Psi_{10} = 6.66$ Pa s^2 in the limit of zero shear rate. Table 2 lists the parameters used to compute the material properties.

The Rouse–Zimm model accurately predicts the frequency response of the measured dynamic rigidity $2\eta''(\omega)/\omega$. At medium frequencies, $1/\lambda_z \ll \omega \ll 1/\lambda_{ps}$ the slope of this data allows an approximate determination of the hydrodynamic interaction parameter h^* [40]. In the limit $h^* = 0$, the free-draining Rouse model incorporates no hydrodynamic interaction and $2\eta''/\omega \sim \omega^{-3/2}$, whereas in the Zimm (non-free-draining) limit $h^* \approx 0.25$ and $2\eta''/\omega \sim \omega^{-4/3}$. For the present data $2\eta''/\omega \sim \omega^{-1.44}$ suggesting from the approximate solution of Thurston that $h^* \approx 0.1$ [41]. At low frequencies ($\omega \leq 0.01$ rad/s) the fluid is essentially Newtonian and the phase angle $\delta \to 90^\circ$ so that significant experimental error is expected in the measurements. However, at high frequencies ($\omega \geq 1000$ rad/s) the Zimm model predictions deviate from the experimental measurements due to the small but finite elasticity of the oligomeric solvent. This additional elasticity can be modeled by an extra Maxwell element for the solvent with a relaxation time $\lambda_{ps} \simeq 2.5 \times 10^{-4}$ s which is in good agreement with the range of values reported by Mackay and Boger [42] and Quinzani et al. [19].

The solid line in Fig. 3 represents the predictions of a single FENE-P model for the steady shear data. If the finite extensibility is computed from the molecular weight and radius of gyration of the chain we obtain $L = 93$. The FENE-P model contains no adjustable parameters, however, it is clear that a simple dumbbell model does not capture all of the physics observed at high deformation rates. The asymptotic slope of the expression for $\Psi_1(\dot{\gamma})$ at high shear rates cannot be changed; however, a better fit, meaning that the model crosses through the experimental data and not above it, can be obtained if the extensibility parameter L is reduced to a value of $L = 15$. The much earlier onset of shear-thinning in $\Psi_1(\dot{\gamma})$ observed experimentally is most likely due to hydrodynamic interactions between the beads of the deformed chain which is not captured in the Zimm (pre-averaged) model [43].

Variations in the viscoelastic properties of the test fluid can occur due to thermal fluctuations in the laboratory test environment. To correct for these effects, we employ time-temperature superposition with a shift factor

$$a_T = \frac{\eta_0(T)T_0\rho_0}{\eta_0(T_0)T\rho} \tag{2}$$

Table 2
Parameters characterizing viscometric properties of the 0.025% PS/PS solution

	Notation	Value of parameter
Reference temperature	T_0	298 K
Variable	η_0	22.75 Pa s
	η_s	21.0 Pa s
	λ_{ps}	2.5×10^{-4} s
	h^*	0.1
	M_w	2.25×10^6 g/mol
Calculated	λ_z	3.24 s
	Ψ_{10}	6.66 Pa s^2

Table 3
WLF equation parameters used to fit the temperature dependence of the 0.025% PS/PS solution

Parameter	Value of parameter
T_0	298 K
a	16.4
b	80.5

to adjust the strain rate, normal stress difference and viscosity to a reference temperature of $T_0 = 25^{\circ}$C [44]. For the temperature ranges experienced in the laboratory, we use the WLF equation to determine a_T which has been found to be valid for a wide variety of polymer solutions and melts and has the form

$$\log a_T = \frac{-a(T - T_0)}{b + (T - T_0)} \tag{3}$$

where a and b are constants to be determined [44]. Table 3 gives the values of the constants used to fit the temperature dependence of the 0.025% PS/PS solution to the WLF equation.

2.5. Dimensionless parameters

The relative importance of inertial to viscous effects in the flow is characterized by the Reynolds number. In the present work we define the characteristic Reynolds number based on the flow conditions at the contraction plane as $\mathrm{Re} = 2\rho\langle v_z\rangle_2 R_2/\eta_0$, where $\langle v_z\rangle_2 = Q/\pi R_2^2$ is the average axial velocity through the contraction, Q is the volume flow rate and $\rho = 1.026$ g/cm^3 is the density of the fluid. For all experiments performed the Reynolds number $\mathrm{Re} < 1 \times 10^{-2}$, making it possible to neglect inertial effects and placing these experiments well within the creeping flow regime.

The Deborah number characterizes the relative importance of elastic effects to viscous effects in the flow. To determine the Deborah number we need to select both a characteristic timescale for the flow and a representative measure of the spectrum of relaxation times of the fluid. A characteristic strain rate based on the local flow conditions near the plane of the contraction is defined by $\dot{\gamma} \equiv \langle v_z\rangle_2/R_2$. A characteristic convective time of the flow can then be taken to be $\mathscr{T} \equiv R_2/\langle v_z\rangle_2 = \dot{\gamma}^{-1}$. The simplest choice for the fluid time scale is of course the longest or Zimm relaxation time λ_z determined from the linear viscoelastic measurements. Even though the viscosity does not have a strong rate dependence, the first normal stress coefficient does. It is, therefore, important to note that the relaxation time, which can be calculated from the viscometric properties of the fluid previously determined, is a function of shear rate [44]. In polymer melts, it is customary to use a shear-rate-dependent relaxation time of the form

$$\lambda(\dot{\gamma}) \equiv \frac{\Psi_1(\dot{\gamma})}{2\eta(\dot{\gamma})} \tag{4}$$

The dimensionless product $\lambda(\dot{\gamma})\dot{\gamma}$ is thus equivalent to half the stress ratio [45].

Discrepancies between different estimates of the relaxation time have been discussed at length by Keiller et al. [46]. For scaling purposes, in the present work the characteristic relaxation time of the 0.025% PS/PS solution will be given by the relaxation time evaluated in the limit of zero shear rate.

After substituting for the asymptotic value of Ψ_{10} obtained from the Rouse–Zimm model, the characteristic relaxation time becomes

$$\lambda_0 = \frac{\Psi_{10}}{2\eta_0} = 0.29\lambda_z \frac{\eta_p}{\eta_0} = 0.146\,\mathrm{s} \tag{5}$$

The zero-shear-rate Deborah number expressed with this choice of constant characteristic relaxation time becomes $\mathrm{De} = \lambda_0\dot{\gamma}$. For convenience, we will report the Deborah number in the latter representation for all experiments in this paper. The shear-rate-dependent Deborah number of flow through a 4 : 1 : 4 axisymmetric contraction is expressed as

$$\mathrm{De}(\dot{\gamma}) = \lambda(\dot{\gamma})\dot{\gamma} = \frac{\Psi_1(\dot{\gamma})\langle v_z\rangle_2}{2\eta(\dot{\gamma})R_2} \tag{6}$$

and may also be thought of as a Weissenberg number [29] or recoverable shear because it is a direct estimate of the ratio of the normal stress difference to the total shear stress in the fluid at a given deformation rate $\dot{\gamma}$. We refer to this generically as a stress ratio SR which was used in early publications to report the magnitude of viscoelastic effects in flow through a contraction [45]. Fig. 4 shows a plot of the stress ratio, $\mathrm{SR} \equiv N_1(\dot{\gamma})/\tau_{12}(\dot{\gamma})$, as a function of strain rate to demonstrate the rate dependence of the elastic stress difference in the fluid. The filled circles represent the steady shear viscometric data and the short dashed line represents the linear approximation to the stress ratio if the constant relaxation time is used; $\mathrm{SR}_0 = 2\lambda_0\dot{\gamma}$. The non-monotonicity in the dynamic data is a consequence of the additional

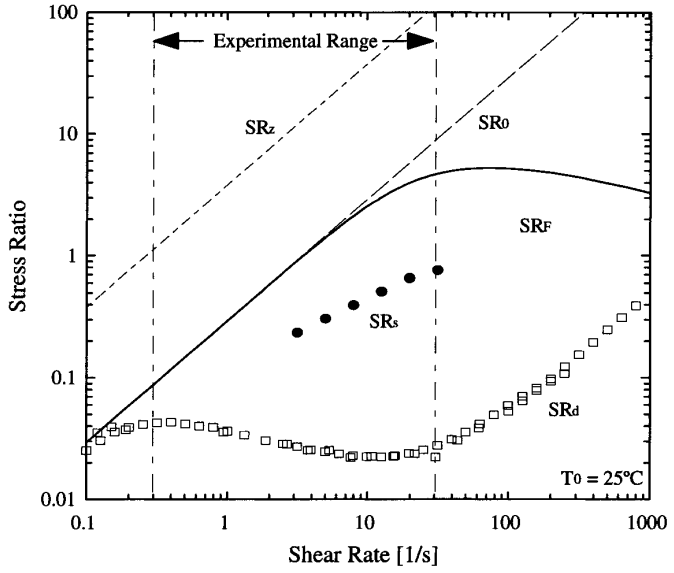

Fig. 4. Various estimates of the stress ratio $\mathrm{SR} \equiv \tau_{xx}/\tau_{yx}$ of the 0.025 wt.% PS/PS solution in steady shear. The data includes: ●, the experimental stress ratio from steady shear data $\mathrm{SR}_s = N_1/\tau_{yx} = \Psi_1\dot{\gamma}/\eta$; □, experimental stress ratio from dynamic data $\mathrm{SR}_d = G'/G'' = \eta''/\eta'$; - -, the stress ratio predicted using the longest relaxation time of the Zimm model $\mathrm{SR}_z = 2\lambda_z\dot{\gamma}$; - -, the stress ratio predicted using the zero-shear-rate relaxation time $\mathrm{SR}_0 = 2\lambda_0\dot{\gamma}$; ———, the stress ratio SR_F predicted by the FENE-P model.

elasticity contributed from the polymeric solvent at high deformation rates. The long dashed line represents the same approximation if the longest 'Zimm' relaxation time were used $SR_z = 2\lambda_z\dot{\gamma}$ and it clearly over predicts the magnitude of elastic effects in the actual test fluid. The solid line represents the stress ratio, SR_F, predicted by the shear thinning FENE-P model. As expected, the experimental values of SR increase with strain rate and begin to approach a maximum around one. At low shear rates, the experimental values of SR approach the linear function SR_0, but throughout the range of deformation rates attained in the experiments, they remain up to an order of magnitude smaller. Even though SR_0 is clearly a better approximation than SR_z it is by no means an ideal description of the actual magnitude of the elasticity in the flow of the 0.025% PS/PS solution and shear-thinning effects must be incorporated to achieve a quantitative description of the data. However, even with a shear-thinning first normal stress coefficient, the FENE-P model does not accurately predict the magnitude of the stress ratio.

3. Experimental results

3.1. Evolution of pressure drop with flow rate

3.1.1. Newtonian pressure drop

The pressure drop of the Newtonian oligomeric polystyrene oil through the 4 : 1 : 4 axisymmetric contraction was measured to serve as a baseline for comparison of the non-Newtonian results and to evaluate the performance of the experimental system. Fig. 5 shows the experimentally measured transient evolution in the pressure drop (ΔP_{24}) across the 4 : 1 : 4 orifice plate for the Newtonian

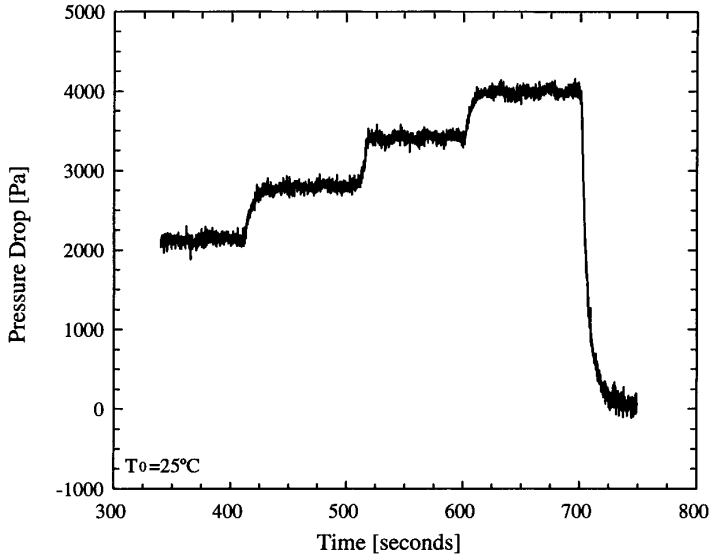

Fig. 5. Pressure drop across the contraction ΔP_{24} for the Newtonian oligomeric PS oil demonstrating the transient response of the system as the characteristic strain rate is stepped from 1.7 to 3.2 s^{-1} in three equal increments of 0.5 s^{-1} and is then dropped to 0 s^{-1}.

polystyrene oil as the characteristic strain rate is stepped from 1.7 to 3.2 s^{-1} in three equal increments of 0.5 s^{-1} and is then reduced to 0 s^{-1}. All values of pressure have been shifted to the value corresponding to a fluid with viscosity η_0 at the reference temperature of $T_0 = 25°C$ using the shift factor a_T discussed in Section 2.4. At a specified flow rate, the pressure drop of a Newtonian fluid in creeping flow is proportional to its viscosity, so the pressure drop should scale with ambient temperature just as its viscosity does. For a non-Newtonian fluid, it would be important to also shift the time axis according to the technique of time–temperature superposition.

Fig. 5 demonstrates that pressure differences resulting from increments of $\Delta\dot{\gamma} \approx 0.5\ s^{-1}$ or smaller are easily discernible above the noise of the system which for the chosen pressure transducers was consistently around ±0.1 kPa (±0.015 psi). For each strain rate shown, the fluid motion approached a steady state after a short system lag of about 10 s. Similar results were observed for the Newtonian PS oil at all strain rates tested ($0.5\ s^{-1} \leq \dot{\gamma} \leq 10\ s^{-1}$) and no flow instabilities were observed under any condition.

In 1891, Sampson first solved the pressure-driven flow of a Newtonian fluid at low Reynolds number through an infinitesimally thin circular hole in an infinite rigid wall using oblate spheroidal coordinates [47]. Of particular interest are Sampson's results for the centerline velocity profile $v_z(z)$ and the pressure drop across the orifice which may be simply expressed in cylindrical coordinates as

$$v_{z,S} = \frac{Q}{2\pi R_2^2}\left(\frac{1}{1+(z/R_2)^2}\right) \tag{7}$$

$$\Delta P_S = \frac{3Q\eta_s}{R_2^3} \tag{8}$$

where Q is the volume flow rate of the fluid and z is the axial distance from the orifice plane. For large contraction ratios $\beta = R_1/R_2 \gg 1$, Sampson's solution should approximate the flow near the plane of the contraction reasonably well. However, because our orifice plate is not infinitely thin and has finite aspect ratio ($L_c/R_2 \neq 0$), there is an additional contribution to the pressure drop. This has been considered analytically by Dagan et. al [48]. Their numerical calculations can be accurately approximated by linearly combining the pressure drop associated with Sampson flow and the pressure drop of the assumed Poiseuille flow through the orifice itself to give

$$\Delta P_D = \frac{Q\eta_s}{R_2^3}\left(3+\frac{8L_c}{\pi R_2}\right) \tag{9}$$

where $L_c = 0.635$ cm is the thickness of the orifice plate.

In the present experiments, $L_c/R_2 = 2$ and the additional pressure drop arising from the latter term in Eq. (9) is not negligible. To eliminate any possible relaxation of the polymer chains in the orifice section, one ideally requires $L_c/R_2 \to 0$; however such a geometry is difficult to experimentally realize and furthermore, from a numerical perspective, the resulting corner singularities would severely compromise viscoelastic flow calculations at high Deborah number. Conversely, in the conventional benchmark of entry flow into a simple contraction ($L_c/R_2 \to \infty$) all of the stored elastic energy is slowly returned to the flow as the stretched molecules advect and relax in the downstream pipe flow and resolution of this slow downstream stress relaxation appreciably increases the domain size and computational expense of simulations.

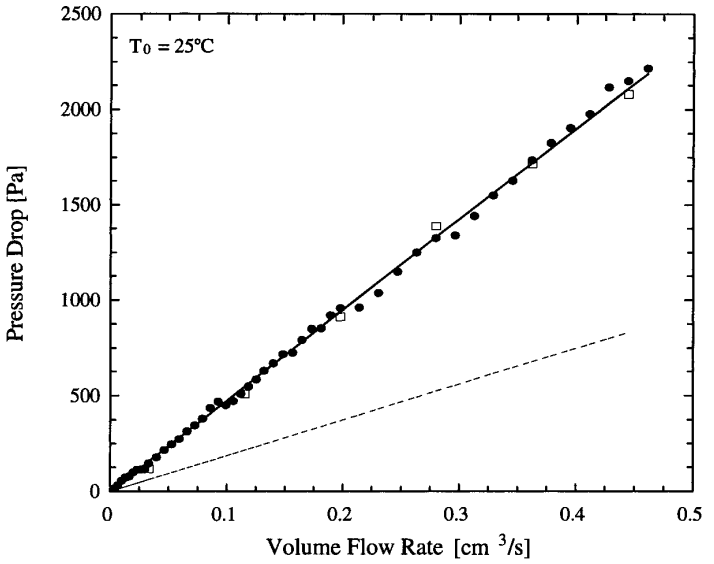

Fig. 6. Extra pressure drop $\Delta P'_{24}$ for the Newtonian oligomeric polystyrene oil through a 4 : 1 : 4 axisymmetric contraction/expansion. The data includes: ●, experimental points taken during forward displacement through the contraction; □, experimental points taken during reverse displacement through the contraction; ———, an approximation to the numerical results of Dagan et. al [48]; - -, the analytical result of Sampson [47].

By selecting a contraction/expansion with a finite value of L_c/R_2, the physical domain of interest is limited to a few radii upstream and downstream of the orifice and it also becomes possible to investigate the effects of varying the local radius of curvature of the re-entrant corner. We shall report on this in later publications. The value $L_c/R_2 = 2$ is in the same range as previous experimental [25] and numerical [31] studies of viscoelastic flows through contraction/expansions.

Fig. 6 is a comparison of the experimentally measured pressure drop $\Delta P'_{24}(Q)$ of the Newtonian PS oil through the 4 : 1 : 4 contraction with the predictions of Sampson and Dagan. Once again the pressure data has been shifted to the reference temperature of $T_0 = 25^\circ$C. For creeping flows of a Newtonian fluid, the velocity field is symmetric in the converging and diverging flows near the contraction plane. Pressure measurements were performed for both forward and backward flows through the contraction to rule out any hysteresis effects. As expected, the pressure drop is linearly proportional to the volumetric flow rate. The Sampson flow prediction is systematically low, but the prediction of Dagan et al. is remarkably good and provides almost an exact fit to the data. Even though the experimentally manufactured orifice plate is only 0.635 cm thick, the additional viscous pressure drop, $8QL_c\eta/\pi R_2^4$, is as large as the contribution from the Sampson converging flow.

An alternative approach commonly used in presenting contraction flow results is to report a *Couette correction* [49] in which the extra pressure drop arising from the orifice is scaled with the wall shear stress in the downstream tube $C = \Delta P'_{ext}/2\tau_w$, where $\tau_w = 4\eta_s\langle v_2\rangle/R_2 = 4\eta_s Q/\pi R_2^3$. For $\beta \to \infty$, the Couette correction for a Newtonian fluid entering an abrupt contraction the Sampson solution thus predicts $C = 0.5(\Delta P_S/2\tau_w) = 3\pi/16 = 0.589$ which is in good agreement with simulations and measurements [50].

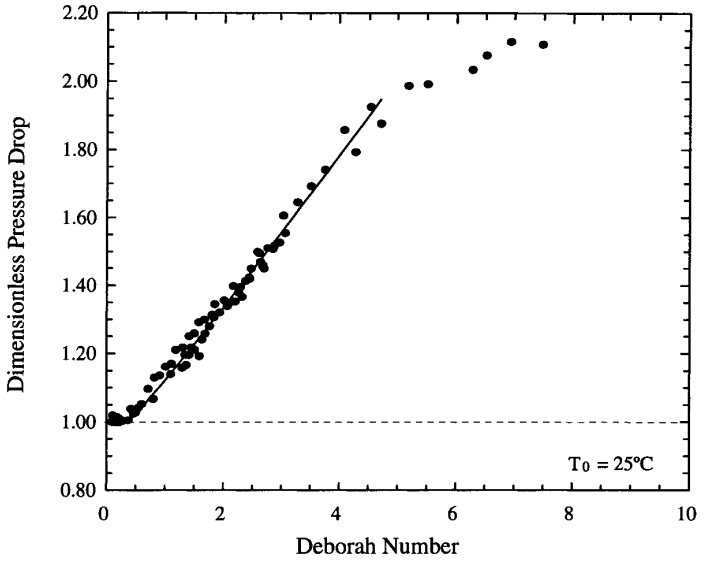

Fig. 7. Dimensionless pressure drop $\mathscr{P}(\mathrm{De}) = \Delta P'_{24}(\mathrm{De}, Q)/\Delta P'_{24}(\mathrm{De}=0, Q)$ of the 0.025 wt.% PS/PS solution across the 4 : 1 : 4 axisymmetric contraction as a function of Deborah number $\mathrm{De} = \lambda_0\dot{\gamma}$. The figure includes: ●, experimental data; ———, linear regression of the form $\mathscr{P} = 1 + 0.2(\mathrm{De} - \mathrm{De}_{\mathrm{cr1}})^{1.05}$.

3.1.2. Non-Newtonian pressure drop

The pressure drop of the non-Newtonian 0.025% PS/PS solution through the 4 : 1 : 4 axisymmetric contraction ($\Delta P'_{24}$) was measured for Deborah numbers in the range $0.06 \leq \mathrm{De} \leq 7.5$. Fig. 7 shows the results of these experiments. The evolution in the Couette correction with increasing Deborah number is commonly reported in numerical calculations [13,51]. However, in the present work, we chose to report values in terms of the dimensionless pressure drop $\mathscr{P}(\mathrm{De}) = \Delta P'_{24}(Q, \mathrm{De})/\Delta P'_{24}(Q, \mathrm{De}=0)$, where $\Delta P'_{24}(Q, \mathrm{De}=0)$ is the best fit to the Newtonian pressure drop data described in Section 3.1.1. In the limit $\mathrm{De} \to 0$ we therefore expect $\mathscr{P} \to 1.0$. The scatter in the data is due for the most part to an uncertainty of $\pm 0.1^{\circ}\mathrm{C}$ in the temperature measurements which leads, through a propagation of error analysis, to a 2% uncertainty in both the dimensionless pressure drop and the Deborah number at each point. At low Deborah numbers, when the elasticity of the fluid is negligible, one would expect the fluid to be Newtonian with a dimensionless pressure drop close to one, as confirmed in Fig. 7. As the Deborah number is increased, the experiments show a marked increase in the dimensionless pressure drop beginning at a critical Deborah number of $\mathrm{De}_{\mathrm{cr1}} = 0.4$. This value is quite close to a Deborah number of $De = 0.5$, at which *coil-stretch transition* occurs in a homogeneous extensional flow. Beyond this critical point, the dimensionless pressure drop becomes a monotonically increasing function of the Deborah number of the form $\mathscr{P} = 1 + 0.2(\mathrm{De} - \mathrm{De}_{\mathrm{cr1}})^{1.05}$ for $\mathrm{De} \leq 5.0$. As the Deborah number is increased still further, the dimensionless pressure drop appears to saturate, plateauing at a value of $\mathscr{P} \approx 2.1$.

The increase in the pressure drop above the Newtonian result for flows above the critical Deborah number $\mathrm{De}_{\mathrm{cr1}}$ is consistent with previous experimental studies for flow of polyacrylamide-based flows across a 4 : 1 : 4 orifice [25] which also showed a large increase and ultimate saturation in the dimensionless pressure drop $\mathscr{P}(\mathrm{De})$. Large additional pressure drops have also been observed in entry flows of polymer solutions in 4 : 1 contractions [16,24,26,27]. By contrast, numerical studies for both

the 4 : 1 contraction [13,30] and the 4 : 1 : 4 orifice [31] show that for creeping flows of simple viscoelastic models such as the FENE-P and Oldroyd-B equations the dimensionless pressure decreases at moderate $De \sim O(1)$. In the case of FENE-P dumbbell calculations, small increases in the dimensionless pressure drop are observed as the molecules approach maximum elongation, but Szabo et al. report a maximum increase of approximately 10% at a Deborah number of $De = 9.5$ for a finite extensibility of $L = 5$. Simulations of viscoelastic flows into 4 : 1 contractions with multimode nonlinear models do show increases in the Couette correction with Deborah number [29,51], however, this is associated primarily with shear-thinning effects in the viscosity arising from the decrease in the scaled wall shear stress in the downstream tube at high shear rates. Such effects are not possible in the present work due to the replacement of the capillary tube downstream of the contraction plane with a diverging flow and the constant viscosity of the PS solvent. The experimentally observed increase in the pressure drop must thus arise from viscoelastic effects associated with the rapid converging and diverging flow.

While visualizing the flow of the 0.025% PS/PS solution, a slow non-symmetric pulsating of the enlarged corner vortices was observed at large Deborah numbers. This periodic growth and decay of the corner vortex is associated with the onset of a supercritical Hopf bifurcation. Fig. 8 shows the temporal variation in pressure drop $\Delta P_{24}(t)$ as the flow rate and the Deborah number are increased from $De = 0.6$ to $De = 4.5$. Oscillations in the pressure drop data become visually apparent for Deborah numbers larger than $De > 2.8$ and the magnitude of these fluctuations increase dramatically with increased Deborah number. Similar pressure drop fluctuations arising from elastic instabilities in strong converging/diverging flows such as flow through banks of cylinders have been previously observed.

A fast Fourier transform (FFT) was performed on the pressure drop data to determine the frequency of the vortex oscillations and to determine the critical Deborah number for the onset of this elastic flow instability. Fig. 9 shows the power spectral density of the signal as De is increased. Fig. 9 (a) shows the

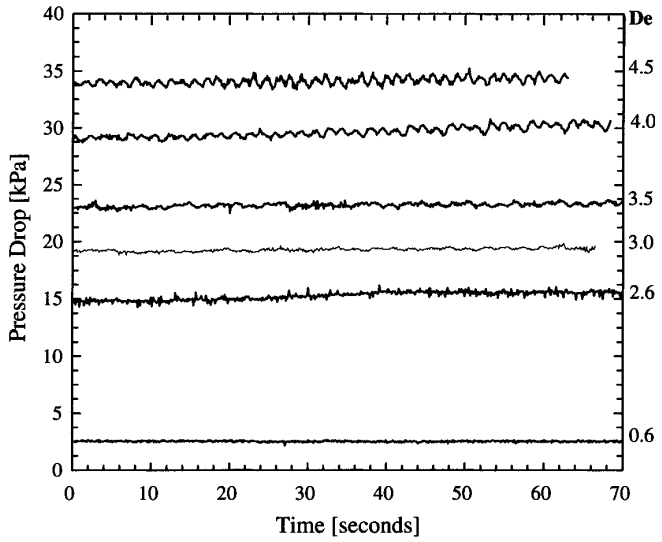

Fig. 8. Pressure drop (ΔP_{24}) across the contraction plane as a function of time for the 0.025 wt% PS/PS solution at various Deborah numbers. The oscillations in the pressure show the onset of a flow instability at a critical Deborah number of $De_\ell = 2.6 \pm 0.1$.

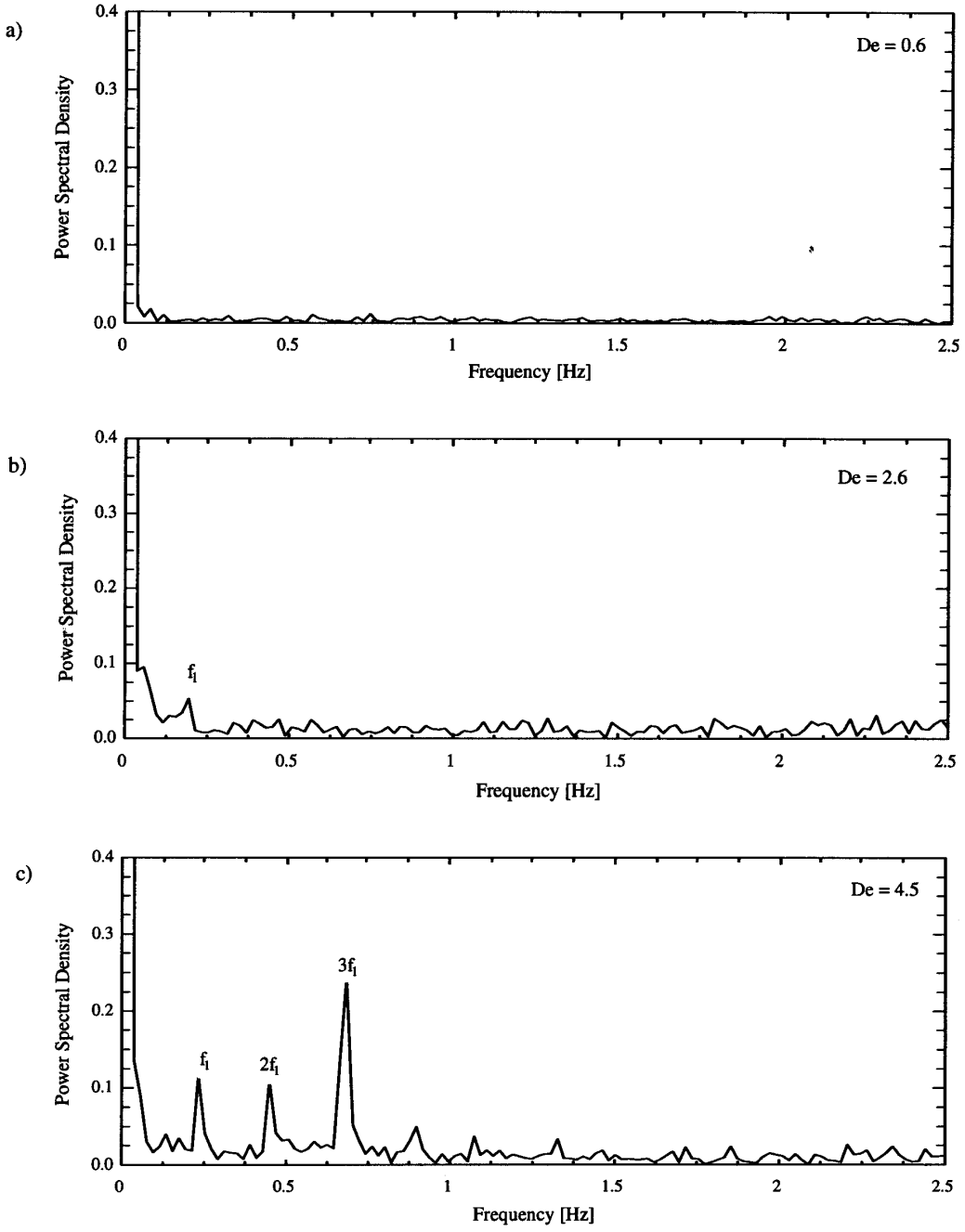

Fig. 9. Power spectral density plots of pressure drop ΔP_{24} for 0.025 wt%. PS/PS solution at three different Deborah numbers (a) De = 0.6, (b) De = 2.6 and (c) De = 4.5 showing the onset of a supercritical elastic flow instability.

Fourier spectrum for De = 0.6; the pressure drop data is clearly stable in time, with no peaks discernable above the background noise. Fig. 9(b) indicates the first signs of the onset of a local flow instability at a critical Deborah number for vortex oscillation of $De_\ell = 2.6 \pm 0.1$. A single small peak at

a the fundamental oscillation frequency $f_1 = 0.20$ Hz can be discerned above the noise floor. At this critical Deborah number, the oscillations observed in the pressure drop are not observable in the global flow patterns or in the vortex structure. However, at a second critical Deborah number $De_{\ell} = 2.8 \pm 0.1$, onset of a global elastic instability is characterized by unsteady flow patterns and an asymmetric precessing of the corner vortices. As the Deborah number is further increased, the intensity of the pressure drop fluctuations grows in amplitude, the frequency of oscillations slowly increases and higher harmonics of the fundamental frequency begin to appear. At a Deborah number of De = 4.5, the FFT in Fig. 9 (c) contains two strong harmonics of the fundamental frequency ($f_1 = 0.23$ Hz) at $f_2 = 2f_1 = 0.45$ Hz and $f_3 = 3f_1 = 0.68$ Hz.

Similar supercritical Hopf bifurcation were first observed by Muller while studying the flow a PIB/PB/K Boger fluid through a 4 : 1 contraction [52]. However, in contrast to our present observations and the detailed studies of McKinley et al. using a PIB/PB/C14 Boger fluid [15], Lawler et al. found the flow returned to a steady two-dimensional motion as the Deborah number was increased further. The flow of the 0.025% PS/PS solution used in the present study remains time-dependent for all Deborah numbers above De_{ℓ}.

3.2. Flow visualization

Flow visualization was used to observe vortex growth and development in the upstream tube with increasing Deborah number. Fig. 10 shows streak images created using the technique discussed in Section 2.2. The first image shows the particle streamlines for a low Deborah number, De = 0.05. At such low flow rates, the 0.025% PS/PS solution is essentially Newtonian and small weak recirculation zones or 'Moffatt vortices' (with characteristic concave dividing streamlines) can be seen in the stagnant corners just upstream of the contraction plane. As the Deborah number is increased, the corner vortices increase in size and strength. The presence or the absence of a lip vortex has been noted in many different studies and depends on the both the fluid used and the contraction ratio through which it is forced [10]. In contrast to the results of other contraction flow experiments with PIB/PB fluids [10,15], for the PS/PS fluid in the 4 : 1 : 4 contraction/expansion we do not observe the formation of a separate and distinct time-dependent lip vortex. Instead, the corner vortex 'fingers' out towards the

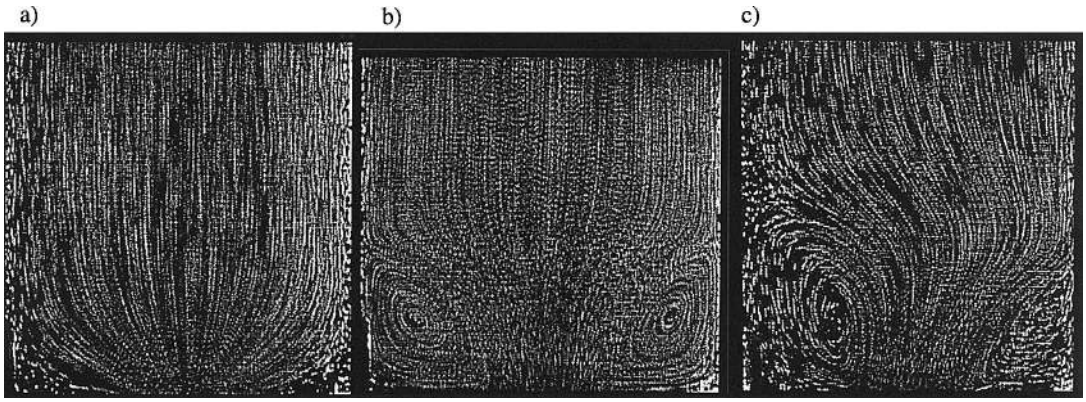

Fig. 10. Streak images of flow upstream of the contraction for Deborah numbers of (a) De = 0.05, (b) De = 2.6 and (c) De = 5.5 showing streamline patterns and upstream vortex growth.

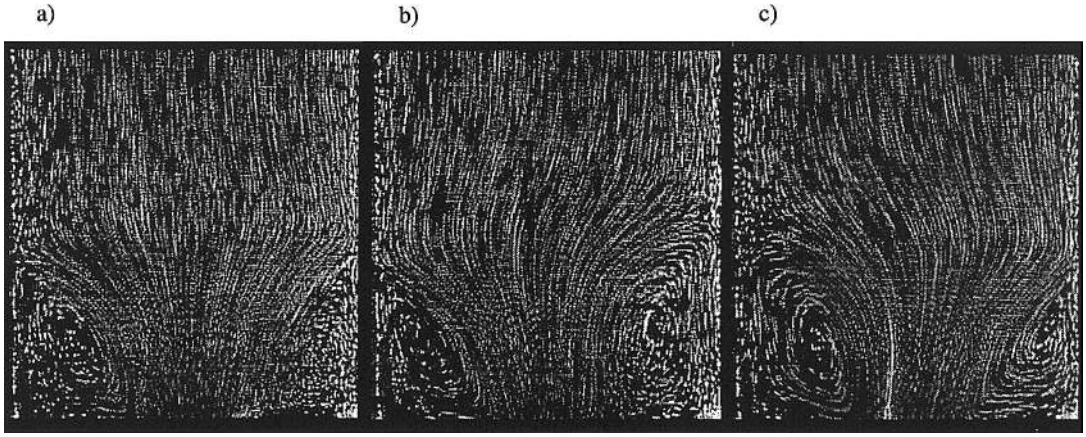

Fig. 11. Streak images of the flow upstream of the contraction plane demonstrating the precession of the upstream corner vortex for a Deborah number of De = 4.7 at times corresponding to fractions of the fundamental period of oscillation, $1/f_1 = 5.1$ s, (a) $t = t_0$, (b) $t = t_0 + 1/(4f_1)$ and (c) $t = t_0 + 3/(4f_1)$.

contraction entrance, the dividing streamline becomes convex and then proceeds to grow upstream. Fig. 10 (b) shows the streak lines for a Deborah number of De = 2.6. This flow demonstrates the large, convex vortices indicative of highly elastic converging flow and it also corresponds to the critical value of Deborah number for the onset of the local instability. Even though the instability is present in the pressure measurements by this point, there is no noticeable effect on the streak line images, at least for this time exposure of $\Delta t = 1.3$ s which is somewhat smaller than the characteristic period of the pressure oscillations. This is not the case for the streak lines in Fig. 10 (c) which indicate the presence of a global instability in the flow at a Deborah number of De = 5.5 and clearly show the non-symmetric corner vortex. Visual observations of this vortex show that the vortex boundary precesses in the azimuthal direction so that fluid elements follow a helical path into the orifice.

The precessing of the upstream vortex is demonstrated more clearly in Fig. 11 which shows three streak images taken at a Deborah number of De = 4.7 at various times throughout one period of the vortex oscillation cycle. Fig. 11 (a) shows a symmetric flow field at time $t = t_0$. As seen in Fig. 11 (b), after an additional one quarter of the fundamental period of vortex oscillation, $t = t_0 + 1/(4f_1)$, the symmetry is broken by a marked increase in the size of the right-hand vortex and a substantial decrease in the size of the left-hand vortex. If the time is increased by an additional half period to $t = t_0 + 3/(4f_1)$, the anti-symmetric vortex structure mirrors itself about the centerline of the upstream tube. The precession of the large vortex to the left of the upstream tube and the corresponding shift of the small vortex to the right hand side can be readily distinguished in Fig. 11 (c).

Quantitative measurements of the vortex size were extracted digitally from the streak images of each experiment. Fig. 12 shows the evolution in the dimensionless reattachment length $\chi \equiv L_v/2R_1$ and the dimensionless coordinates of the vortex center $\zeta \equiv Z_v/2R_1$ and $\xi \equiv R_v/2R_1$ as a function of Deborah number. At low Deborah numbers the dimensionless reattachment length is constant with the expected value for creeping Newtonian flow, $\chi_{\text{Moffatt}} \approx 0.17$. As the flow rate is increased the reattachment length and the axial location of the vortex center begin to increase monotonically with Deborah number. The radial location of the vortex center moves inward from the center of the tube to a radial position $R_v = 0.56R_1$ where it saturates and remains constant as the vortex grows upstream with

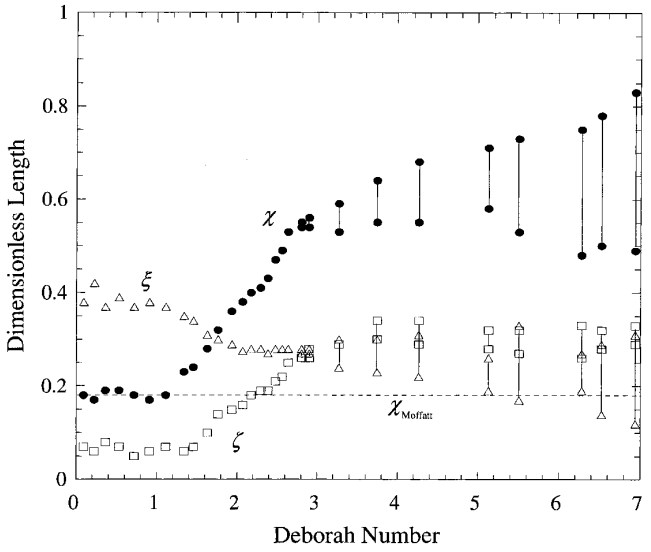

Fig. 12. Characteristics of the upstream vortex enhancement as a function of Deborah number: ●, vortex reattachment length, $\chi = L_v/2R_1$; △, radial location of the vortex center, $\xi = R_v/2R_1$; □, the upstream location of the vortex center, $\zeta = Z_v/2R_1$.

increasing Deborah number. Once the critical Deborah number for the onset of the global elastic instability is reached, the vortex begins to oscillate in size.

The trends of this data agree with previous experimental results for contraction flows of other polymer solutions that do not lead to formation of lip vortices [10,15,16,20]. Although, to our

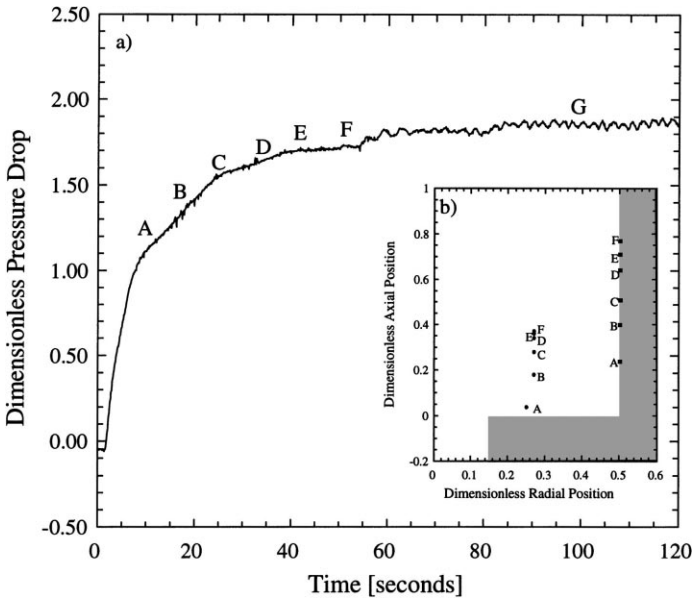

Fig. 13. Transient dimensionless pressure drop (a) and vortex size (b) data for the flow of the 0.025 wt% PS/PS solution through an axisymmetric contraction at a Deborah number of De = 4.7 from start-up to the onset of an elastic flow instability.

knowledge, this is the first time that the location of the corner vortex center has been reported experimentally, it has been reported for numerical work in the past [31]. In the work of Szabo et al. the upstream vortex which started as a small Newtonian vortex, began to grow outwards toward the re-entrant corner and then proceeded to grow upstream as the Deborah number is increased. Except for the 'fingering' of the corner vortex towards the re-entrant corner at the onset of vortex enhancement, the

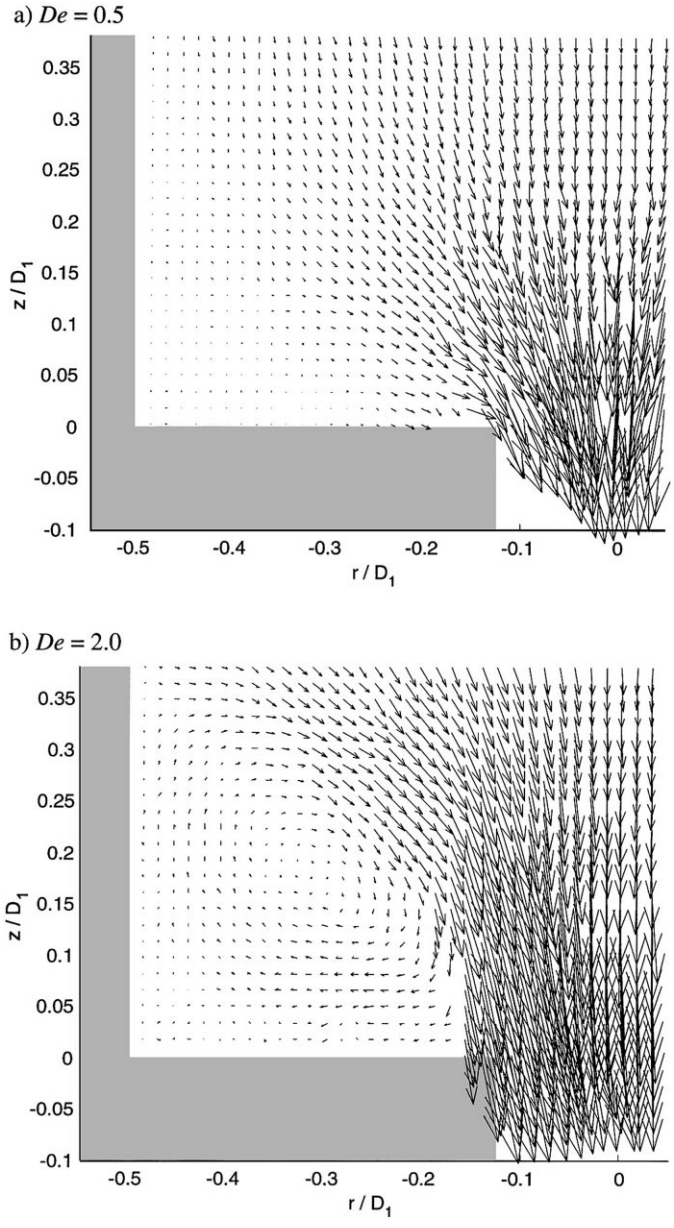

Fig. 14. PIV vector fields for the flow of the 0.025 wt.% PS/PS solution into the axisymmetric contraction at Deborah numbers of De=0.5, 2.0, 2.5 and 3.5.

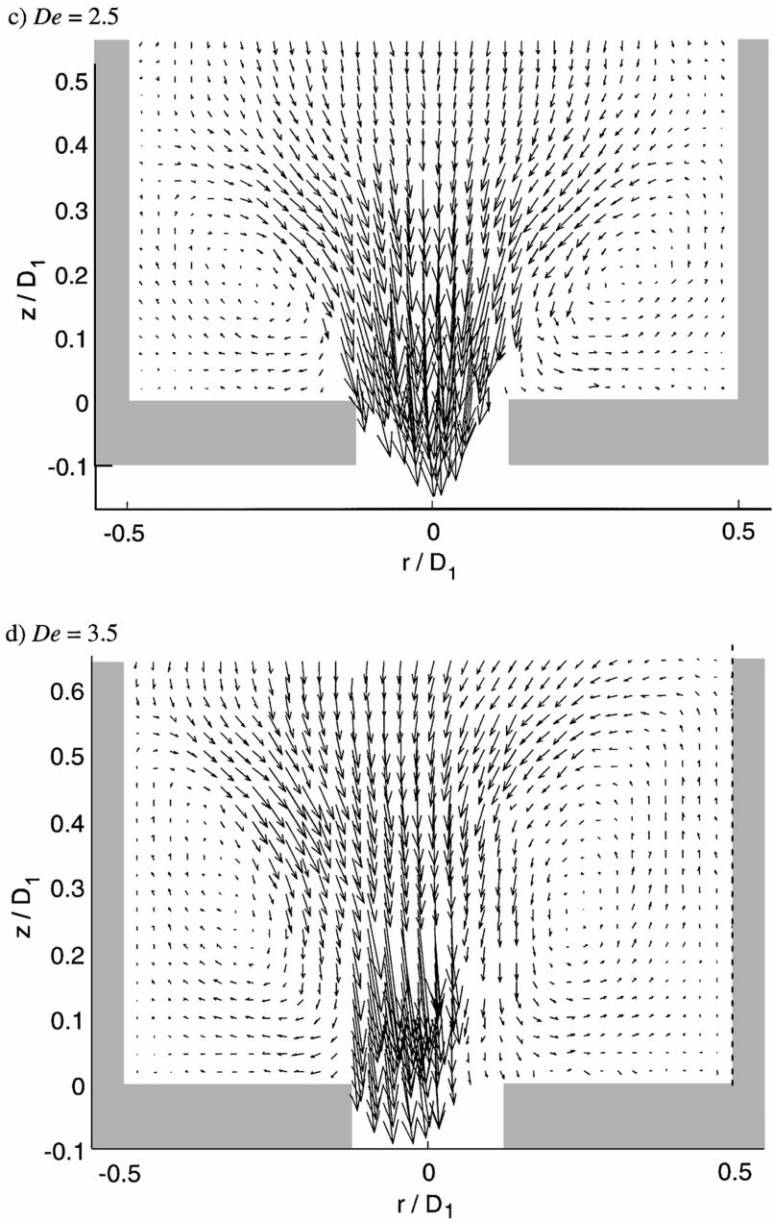

Fig. 14. (*Continued*)

vortex behavior reported by Szabo et al. is qualitatively similar to the vortex growth behavior observed in the present experiments.

Fig. 13 (a) shows the transient dimensionless extra pressure drop $\mathscr{P}(t)$ following a step increase in the driving piston velocity from initial start-up until the onset of the elastic flow instability for a flow at a Deborah number of De = 4.7. Seven points have been labeled on the dimensionless pressure drop curve and the corresponding vortex center and reattachment points have been plotted in Fig. 13 (b). Mirrored

by the development of the corner vortex, the dimensionless pressure drop evolves in four distinct regions: a sharp jump in dimensionless pressure drop attributable to the start-up of the experimental system for times $t < A$, a region of fast growth in the dimensionless pressure drop and vortex size for times $A < t < C$, a region of slower changes in dimensionless pressure drop and vortex growth that approaches a local steady-state value of pressure drop and vortex size for times $C < t < F$ and, finally, the onset and growth of the small amplitude oscillations in dimensionless pressure drop and vortex size associated with the elastic flow instability for $t > F$. This evolution of the dimensionless pressure drop and the corner vortex is in good qualitative agreement with the numerical simulations of Szabo et al. [31].

3.3. Digital particle image velocimetry

We have also used the digital images of the particle motions near the contraction plane to compute instantaneous DPIV vector fields. It should be noted that there are several difficulties encountered in the implementation of DPIV technique which need to be addressed in future work. The principal difficulty arises from the limited dynamic range of digital particle image velocimetry. For particle displacements on the order of the correlation window size there is a progressive loss of information as seed particles are swept out of the correlation region. Conversely, increasing the window size leads to a decrease in the spatial resolution that can be attained. This 'uncertainty principle' is of particular importance near the contraction plane, and the loss of particles into the throat results in uncorrelated regions as the Deborah number gets larger. Since our primary focus in the present work is on the global characteristics of the upstream vortex rather than the quantitative features of the converging flow very near the throat we have selected a field of view that can resolve the entire width of the upstream tube.

Fig. 14 shows the results of DPIV for four Deborah numbers, $De = 0.5$, 2.0, 2.5 and 3.5. The vectors are scaled such that an arrow of length $\Delta z/2R_1 = 0.1$ corresponds to a velocity of $v_z/\langle v_z\rangle_2 = 0.2$ for Fig. 14a,b and $v_z/\langle v_z\rangle_2 = 0.1$ for Fig. 14c,d.

At low Deborah numbers, the corner vortex is so weak that it cannot be resolved readily by the DPIV algorithm, but as the Deborah number is increased, the vortex grows in strength and its structure is easily captured. Similar DPIV images have been generated for all Deborah numbers at which flow visualizations discussed in Section 3.2 were reported. It is hoped that these vector fields will be useful in a detailed comparison between experimental and numerical work in the future.

4. Summary and discussion

In this work, we have measured the additional pressure drop associated with strong extensional flow of a monodisperse polymer solution through a 4 : 1 : 4 axisymmetric contraction/expansion. This large additional pressure drop is not predicted by existing numerical computations with simple dumbbell models. Possible reasons for these discrepancies may lie in the way different models treat polymer chains. In quasilinear dumbbell models, such as the Oldroyd-B model, the entropic elasticity of the Hookean spring can store considerable amounts of energy as a polymer molecule is extended. In a Lagrangian unsteady flow such as flow through an orifice, a dumbbell is accelerated and undergoes a transient uniaxial elongation, absorbing energy as the polymer chain unravels. The stored energy is then released downstream of the contraction as the polymer chain rapidly relaxes under biaxial expansion. The result is a decrease in the global pressure drop because a portion of the energy lost in the case of a Newtonian fluid is returned to the flow. If finite extensibility is added to the dumbbell model, similar

behavior is observed until the chains approach full extension; beyond this point, the polymer chains behave more like rigid rods and the additional viscous drag on the polymers increases the computed pressure drop across the contraction. However, simulations with the FENE-CR model indicate that this effect is insufficient to account for the huge increases in pressure drop across the contraction seen in this work and in the earlier work of Cartalos and Piau [25].

These discrepancies between the numerical and the experimental work in a prototype complex flow support the observations made in uniaxial transient elongation by Doyle et al. of an additional dissipative contribution to the polymeric stress manifested in the form of a stress-conformation hysteresis [2]. This hysteresis would result in an additional dissipative stress term present during the rapid extension of the polymer molecules. The first theoretical considerations of such phenomena were made by Ryskin [6] who analyzed the pressure drop measurements of King and James [53] for dilute polymer solutions flowing in a conical entrance region at high Reynolds number. In the resulting 'yo-yo' model, the chains are envisaged to unravel in a similar manner to a yo-yo with the coiled regions near the end connected by a central rigid rod. Viscous drag on the elongating rod results in a dissipative polymeric contribution that increases linearly with the deformation rate $\dot{\varepsilon}$. No general constitutive equation was formulated by Ryskin, however, on the basis of Brownian dynamic simulations, Rallison [3] recently proposed one form for the additional dissipative stress

$$\boldsymbol{\tau}^d \propto \eta_2 \left[\frac{(\boldsymbol{A} : \dot{\boldsymbol{\gamma}})\boldsymbol{A}}{\mathrm{Tr}\boldsymbol{A}} \right] \tag{10}$$

where $\boldsymbol{A} = \langle \boldsymbol{Q}\,\boldsymbol{Q} \rangle$, is the ensemble average of the mean end-to-end contour length of the molecule and η_2 is the additional contribution to the viscosity.

In a very recent work, Yang and Khomami [54] have computed viscoelastic flow past a sphere – another benchmark flow involving rapid stretching and relaxation – using the full FENE model and do not observe enhancement in macroscopic quantities such as the drag coefficient despite the presence of 'distributional hysteresis'. To capture such effects it may thus be necessary to resolve the internal dynamical structure of the chains that has been observed by Perkins et al. [1] through simulations with bead-rod chain models that can capture such 'configurational hysteresis'.

Although it is not possible in a complex nonhomogeneous flow such as creeping flow through a contraction/expansion to readily estimate the additional pressure drop arising from contributions to the polymeric stress tensor of the form in Eq. (10), it is worth noting that the additional pressure drop $\mathscr{P}$ (i.e. the pressure increase beyond that associated with the linear, Newtonian change in $\Delta P'_{24}(Q)$ with increasing flow rate, Q) does increase linearly with the Deborah number. The combined pressure drop, vortex size and DPIV measurements for a well characterized dilute monodisperse polymer solution should make the data presented in this paper suitable for a quantiative comparison with future numerical simulations using such models.

It is also possible to use the pressure drop data presented above to estimate an approximate extensional viscosity using the technique developed by Cogswell [22] which assumes the fluid viscosity to follow a power-law profile in shear ($n = 1$ in our case). The resulting equations are of the form

$$\bar{\eta} = \frac{9\pi}{64}\frac{R_2^3}{Q}\left(\frac{\Delta P_{\mathrm{ext}}}{2\tau_{\mathrm{w}}}\right)\Delta P_{\mathrm{ext}} \tag{11}$$

$$\dot{\varepsilon} = \frac{4}{3\pi}\frac{Q}{R_2^3}\left(\frac{2\tau_{\mathrm{w}}}{\Delta P_{\mathrm{ext}}}\right) \tag{12}$$

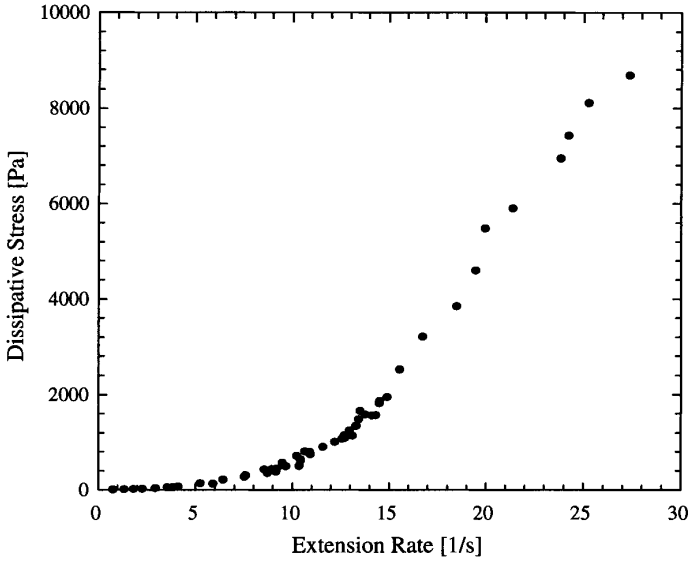

Fig. 15. Estimate of the dissipative stress $\Delta\tau^{\mathrm{d}}$ as a function of the extension rate for the flow of a 0.025 wt% PS/PS solution through a 4 : 1 : 4 axisymmetric contraction at a constant Hencky strain of $\varepsilon = 2.77$.

Cogswell's extensional viscosity determined using the above expression can be approximated as a linear combination of the extensional viscosity of the solvent η_{s} and the extensional viscosity resulting from the dissipative contribution to the polymeric stress $\bar{\eta}^d$, $\bar{\eta} = 3\eta_{\mathrm{s}} + \bar{\eta}^d(\dot{\varepsilon})$. For a rapid contraction/expansion we know that the additional pressure drop arising from the FENE-like elastic stretching is essentially zero [31]. We can now calculate an approximate dissipative stress from the dissipative extensional viscosity and the extension rate $\Delta\tau^d = \dot{\varepsilon}\bar{\eta}^d$. Fig. 15 shows a plot of the approximate dissipative stress $\Delta\tau^{\mathrm{d}}$ as a function of the extension rate $\dot{\varepsilon}$. As expected, the dissipative stress starts at zero and Coggswell's analysis correctly predicts. $\bar{\eta} \approx 3\eta_{\mathrm{s}}$ for low extension rates where the fluid is Newtonian. As the extension rate is increased, the dissipative stress begins to increase slowly until an extension rate of $\dot{\varepsilon} = 14\ \mathrm{s}^{-1}$ after which it grows linearly with extension rate through the onset of the elastic flow instability (at $\dot{\varepsilon} = 17.8\ \mathrm{s}^{-1}$) and through the plateau of the dimensionless pressure drop. This estimate of the dissipative stress can be compared with the values given by Orr and Sridhar who experimentally determined the dissipative stress of PIB/PB at various extension rates and Hencky strains from transient uniaxial extension measurements. The total Hencky strain experienced by a fluid element moving along the centerline of the 4 : 1 axisymmetric contraction region from far upstream to the middle of the throat is given by

$$\varepsilon \equiv \int_0^{t_1} \dot{\varepsilon}\, \mathrm{d}t = \int_{v_z(-\infty)}^{v_z(z=1/2L_c)} \frac{\mathrm{d}v_z}{v_z} = \ln(\beta^2) = 2.77 \tag{13}$$

if we assume a fully developed Poiseuille flow in the throat. Thus the dissipative stress calculated here should be compared with experiments of Orr and Sridhar conducted at Hencky strains of $\varepsilon = 2.77$. Unfortunately, at such a low Hencky strain, the experimental strain rates used by Orr and Sridhar were

not large enough ($\dot{\varepsilon} < 5\ s^{-1}$) to demonstrate any substantial dissipative stresses in either our experiments (Fig. 15) or theirs. However, the dissipative stress is expected to be a function of *both* the extension rate and the Hencky strain, and we can therefore qualitatively compare the two sets of experimental results; each of which tend to increase with extension rate and show maximum dissipative stresses within the experimental range on the order of O (10^4 Pa) [7].

It is important to note that the enhanced pressure drops measured experimentally are not directly connected with the onset of any elastic instabilities. The dimensionless pressure drop begins to increase monotonically with Deborah number at $De = 0.4$ while the onset of local elastic instability does not occur until a Deborah number of $De_\ell = 2.6$. Thus, regardless of whether a numerical simulation can successfully predict the onset of an elastic instability, the chosen constitutive model should still be able to predict the large extra pressure drops associated with the steady motion of non-Newtonian behavior of a dilute polymeric solution before any flow instabilities occur. In fact, we note that in our experiments at controlled displacement rates, the onset of elastic instability in the converging flow of a PS/PS Boger fluid is associated with a lowering in the rate of increase in pressure driving force required. In fluids such as dilute polymer solutions with large contributions to the dissipative stress, the elastic instabilities observed in contraction flows may thus be directly connected to this additional coupling between the conformation (A), the local deformation rate ($\dot{\gamma}$) and the resulting stress (τ). Certainly the magnitude of this additional polymeric stress may be expected to modify the local kinematics in the entry flow region and may help to explain why different Boger fluid formulations (eg. PAA/CS/water, PS/PS and PIB/PB systems) exhibit such different patterns of vortex growth in a 4 : 1 contraction. This may also account for dynamic differences in the flow observed with such fluids in other complex flow geometries; for example the large variations in the evolution of drag coefficient C_D (De) of a sphere sedimenting in a PAA, PS or PIB Boger fluid [33,55]. To investigate such effects further it is necessary to measure the dimensionless pressure drops $\mathscr{P}$(De) in different contraction ratios and for different fluids. We hope to report on such observations in the future. The pressure drop measurements and DPIV measurements coupled with the use of a monodisperse, well-characterized fluid should also make this set of experiments amenable to comparison with numerical work in this benchmark geometry.

Acknowledgements

The authors wish to acknowledge financial support from NASA under grant NAG3-1793, Professor H.A. Stone of Harvard University for making us aware of Sampson's analytical solution and Professor D.P. Hart of MIT for the use of his DPIV algorithm.

References

[1] T.T. Perkins, D.E. Smith, S. Chu, Science 276 (1997) 2016–2021.
[2] P.S. Doyle, E.S.G. Shaqfeh, G.H. McKinley, S.H. Spiegelberg, J. Non-Newtonian Fluid Mech. 76 (1998) 79–110.
[3] J.M. Rallison, J. Non-Newtonian Fluid Mech. 68 (1997) 61–83.
[4] G. Lielens, P. Halin, I. Jaumain, R. Keunings, V. Legat, J. Non-Newtonian Fluid Mech. 76 (1998) 249–279.
[5] E.J. Hinch, J. Non-Newtonian Fluid Mech. 54 (1994) 209–230.
[6] G. Ryskin, J. Fluid Mech. 178 (1987) 423–440.
[7] J. Remmelgas, L.G. Leal, N.V. Orr, T. Sridhar, J. Non-Newtonian Fluid Mech. 76 (1997) 111–135.

[8] D.V. Boger, K. Walters, Rheological Phenomena in Focus, Elsevier, New York, 1993.
[9] O. Hassager, J. Non-Newtonian Fluid Mech. 29 (1988) 2–5.
[10] D.V. Boger, Ann. Rev. Fluid Mech. 19 (1987) 157–182.
[11] S.A. White, A.D. Gotsis, D.G. Baird, J. Non-Newtonian Fluid Mech. 24 (1987) 121–160.
[12] D.V. Boger, R.J. Binnington, J. Rheol. 38 (1994) 333–349.
[13] P.J. Coates, R.C. Armstrong, R.A. Brown, J. Non-Newtonian Fluid Mech. 42 (1992) 141–188.
[14] B. Purnode, M.J. Crochet, J. Non-Newtonian Fluid Mech. 65 (1996) 269–289.
[15] G.H. McKinley, W.P. Raiford, R.A. Brown, R.C. Armstrong, J. Fluid Mech. 223 (1991) 411–456.
[16] D.V. Boger, R.J. Binnington, J. Non-Newtonian Fluid Mech. 35 (1990) 339–360.
[17] G. Mompean, M. Deville, J. Non-Newtonian Fluid Mech. 72 (1997) 253–279.
[18] J.D. Ferry, Viscoelastic Properties of Polymers, Wiley/Interscience, New York, 1980.
[19] L.M. Quinzani, R.C. Armstrong, R.A. Brown, J. Rheol. 39 (1995) 1201–1980.
[20] J.A. Byars, R.J. Binnington, D.V. Boger, J. Non-Newtonian Fluid Mech. 72 (1997) 219–235.
[21] Y.W. Ooi, T. Sridhar, J. Non-Newtonian Fluid Mech. 52 (1994) 153–162.
[22] F.N. Cogswell, Polym. Eng. Sci. 12 (1972) 64–73.
[23] D.F. James, G.M. Chandler, J. Non-Newtonian Fluid Mech. 35 (1990) 445–458.
[24] D.M. Binding, K. Walters, J. Non-Newtonian Fluid Mech. 30 (1988) 233–250.
[25] U. Cartalos, J.M. Piau, J. Non-Newtonian Fluid Mech. 45 (1992) 231–285.
[26] G.D. Eisenbrand, J.D. Goddard, J. Non-Newtonian Fluid Mech. 11 (1982) 37–52.
[27] D.F. James, J.H. Saringer, J. Fluid Mech. 97 (1980) 655–671.
[28] C. Beraudo, A. Fortin, T. Coupez, Y. Demay, B. Vergnes, J.F. Agassant, J. Non-Newtonian Fluid Mech. 75 (1998) 1–23.
[29] M. Gupta, C.A. Hieber, K.K. Wang, Int. J. Numerical Meth. in Fluids 24 (1997) 493–517.
[30] R.A. Keiller, J. Non-Newtonian Fluid Mech. 46 (1993) 143–178.
[31] P. Szabo, J.M. Rallison, E.J. Hinch, J. Non-Newtonian Fluid Mech. 72 (1997) 73–86.
[32] A. Mongruel, M. Cloitre, Phys. Fluids 7 (1995) 2546–2552.
[33] M.J. Solomon, S.J. Muller, J. Non-Newtonian Fluid Mech. 62 (1996) 81–94.
[34] B. Khomami, L.D. Moreno, Rheol. Acta 36 (1997) 367–383.
[35] A. Liu, Viscoelastic Flow of Polymer Solutions Around Arrays of Cylinders: Comparison of Experiment and Theory, Ph.D. Thesis, Dept. Chemical Engineering, MIT, 1997.
[36] P. Pakdel, G.H. McKinley, AIChE Journal 43 (1997) 289–302.
[37] G.K. Batchelor, An Introduction to Fluid Dynamics, Cambridge University Press, Cambridge, UK, 1985.
[38] D.V. Boger, J. Non-Newtonian Fluid Mech., 3 (1977/78) 87–91.
[39] B.H. Zimm, J. Chem. Phys. 24 (1956) 269–278.
[40] R.G. Larson, Constitutive Equations for Polymer Melts and Solutions, Butterworths, Boston, 1988.
[41] R.B. Bird, R.C. Armstrong, O. Hassager, Dynamics of Polymeric Liquids: Kinetic Theory, Wiley, New York, 1987, vol. 2.
[42] M.E. Mackay, D.V. Boger, J. Non-Newtonian Fluid Mech. 22 (1987) 235–243.
[43] J.J. Magda, R.G. Larson, M.E. Mackay, J. Chem. Phys. 89 (1988) 2504–2513.
[44] R.B. Bird, R.C. Armstrong, O. Hassager, Dynamics of Polymeric Liquids: Fluid Mechanics, Wiley, New York, 1987, vol. 1.
[45] C.J.S. Petrie, M.M. Denn, AIChE J. 22 (1976) 209–236.
[46] R.A. Keiller, J.M. Rallison, J.G. Evans, J. Non-Newtonian Fluid Mech. 42 (1992) 249–266.
[47] R.A. Sampson, Phil. Trans. Roy. Soc. 182 (1891) 449.
[48] Z. Dagan, S. Weinbaum, R. Pfeffer, J. Fluid Mech. 115 (1982) 505–523.
[49] D.V. Boger, R. Gupta, R.I. Tanner, J. Non-Newtonian Fluid Mech. 4 (1978) 238–248.
[50] M.E. Mackey, Y.L. Yeow, D.V. Boger, Chemical Eng. Res. Design 66 (1988) 22–25.
[51] B. Bernstein, K.A. Feigl, E.T. Olsen, J. Rheol. 38 (1994) 53–71.
[52] J.V. Lawler, S.J. Muller, R.A. Brown, R.C. Armstrong, J. Non-Newtonian Fluid Mech. 20 (1986) 51–92.
[53] D.H. King, D.F. James, J. Chem. Phys. 78 (1983) 4749–4754.
[54] B. Yang, B. Khomami, J. Non-Newtonian Fluid Mech., in press.
[55] C. Chmielewski, K.L. Nichols, K. Jayaraman, J. Non-Newtonian Fluid Mech. 35 (1990) 37–49.